Condensation Chemistry of Carbon Stars

Katharina Lodders and Bruce Fegley, Jr.

Planetary Chemistry Laboratory, Department of Earth and Planetary Sciences
Washington University, Campus Box 1169, St. Louis, MO 63130-4899, USA

Abstract. A historical overview about the development of thermodynamic calculations and their application to stellar atmospheres is given. Thermochemical equilibrium chemistry for major and trace elements in carbon star atmospheres is discussed. The calculations indicate TiC, graphite and SiC dust formation within 1-3 stellar radii from the photosphere. Trace element abundance patterns observed in circumstellar SiC grains isolated from meteorites are modeled by fractional condensation. The complementary trace element patterns in SiC grains and those in N-star atmospheres are plausibly explained by fractional condensation during stellar variability cycles.

INTRODUCTION AND A HISTORICAL PERSPECTIVE

The ~4000 known carbon stars form a relatively small group among the late type red stars. Most of the red stars are normal oxygen-rich giants of types G, K or M. In the 1860s Secchi [1] realized that stars with different colors also show different spectra and he recognized a group of red stars with curious spectra, which he termed "class four". By the early 1900s these stars were grouped into spectral classes R and N by Pickering [2,3] at Harvard and the R and N classification came into use in the Henry Draper catalog. The cause of the violet absorption in these peculiar stars was unclear at the time, but it seemed that R stars formed a parallel temperature sequence to normal G and K giants while the cooler N stars were closer to normal M stars and to the small group of S-stars. Spectral analyses by Rufus in 1916 [4] showed the enhanced presence of carbon-bearing molecular lines in R and N stars and the term 'carbon-stars' came into use.

Shortly afterward, Wildt (1929 [5]) started the field of thermodynamic modeling of molecular bands in stellar spectra. Recognizing the overwhelming number of possible compounds present in stellar atmospheres of late type G, M, S, R, and N stars and not having either powerful computers or large thermodynamic databases available, Wildt states 'An die vollständige Berechnung des Gleichgewichts eines solchen "Vielstoffsytems" wie einer Sternatmosphäre ist nicht zu denken' [1] Thus, his calculations were restricted to selected gas phase equilibria.

---

[1] It is inconceivable that a complete equilibrium calculation of a "multi-component" system such as a stellar atmosphere can be performed

Table 1. Thermodynamic Studies of Chemistry in Reduced Cool Stars

Authors(s)	elem.	gases	solids	T (K)	Pressure (Bars)	C/O-ratio	Remarks
Wildt 1929 [5]	6	19	none	2000-8000	$1 - 10^{-12}$		selected gas equilibria for molecular band modeling
Cambresier & Rosenfeld 1933 [6,7]	6	12	none	2000-4500	$\sim(10^{-4} - 10^{-6})$	C/O > 1	selected gas equilibria for molecular band modeling
Wildt 1933 [8]			several				carbides and nitrides are possible condensates
Russell 1934 [9]	5	26	none	2000-6000	$10^{-5} - 10^{-8}$	solar, 1	gas equilibria
Bouigue 1957 [10]	5	14	none	1800-3900	10^{-3}	2	N/C= 0.4, Ti, Zr abund. variable
DeJager & Neven 1957 [11]	4	15	none	2500-6400	$10^{-3} - 10^{-9}$	10, 1000	N/C = 1, 0.1
Cowley 1962 [12]	8	29	none	1900-5000	10^{-2}	solar, 1,2	N/C = 8, Ba, Sr, Zr abund. solar & > solar
Hoyle & Wickramasinghe 1962 [13]	1	4	C	1500-3000	result of calc.	~2.2 (result of calc.)	$C+C_2+C_3$ = C(s), nucleation, growth times
Stanger, cited by Aller 1963 [14]	10	17	none	2500-6400	$10^{-3} - 0.1$	2	N/C = 0.08, Ti, Zr, V
Tsuji 1964 [15]	5	60	C	1000-8400	$100 - 10^{-9}$	5	N/C = 1
Dolan 1965 [16]	15	57	none	2520-6300	$10^{-4} - 0.1$	solar, 1, 2	N/C=solar, dwarfs & giants, variable Zr
Morris & Wyller 1967 [17]	5	36	none	1280-8400	$10^{-2} - 10^{-10}$	solar, 1.5, 2.3, 5.8	N/C = 0.18, 27, 42, 50; otherwise solar
Donn et al. 1968 [18]	4	4	C	1000-2500	$0.01 (- 10^{-8})$	2 (1 - 5)	N/H = 0.02, 10^{-4}, 5×10^{-3}, nucleation
Fix 1969 [19]	4	11	C	1500-2000	10^{-3}	0.97	nucleation, mira variables and grain growth
Fix 1969 [20]	3	11	C	1500-2500	?	1 to 3	nucleation, stellar variability and grain growth
Friedemann 1969 [21]	2	?	SiC	1800	3×10^{-5}		condensation & growth times for SiC
Gilman 1969 [22]	12	80	64	1200-2000	$5 \times 10^{-3} - 5 \times 10^{-7}$	solar to 2	solar abundances, mainly $P=5 \times 10^{-5}$, C, SiC
Tsuji 1973 [23]	36	359	C	1000-6300	$10^{-2} - 10^{-6}$	solar, 2.4	N/C = 0.24, solar abund., no gas-solid equilibrium, case for Si enhancement, mainly $P=10^{-3}$
Salpeter 1974 [24]	?	?	several	500-2500	$0.1 - 10^{-14}$	solar, C/O > 1	nucleation of carbon via hydrocarbons (C_2H_2)
Lucy 1976 [25]	11	36	C	1400-2800	$10^{-2} - 10^{-10}$	1.76	solar, except CNO from Kilston 1975. N/C=0.07
Clegg & Wyckoff 1977 [26]	20	125	C	1000-3600	$10^{-3}, 10^{-6}$	solar to 1.6	gas-equilibria, emphasis on CaCl
Lewis & Ney 1979 [27]	?	?	several	500-2500	$10^{4} - 10^{-12}$	solar to 2	solar abund., graphite nucleation on Fe/Fe_3C
McCabe et al. 1979 [28]	25	124	C, SiC	1250-2820	$10^{-3} - 10^{-11}$	1.76, 5	solar abund., no gas-solid equilibrium, mainly $P=10^{-4}$
Clegg 1980 [29]	20	125	C	1000-4000	?	1.05,1.01,1.76,5,10,40	carbyne, cyanoacetylene
Lafont et al. 1982 [30]	6?	?	SiC?	700-2000	$2.6 \times 10^{-6} - 3.2 \times 10^{-7}$	1.1, 2	N/C = solar, no gas-solid equilibrium
Shmeld et al. 1985 [31]	6	94	C, SiC	1000-2000	$10^{-3} - 10^{-6}$	1.2, 1.5, 2, 3, 5	N/C = 0.1, 0.2, 0.33, 0.5, 0.67, 0.83, 2, polyynes
Shmeld 1985 [32]	6	94	C, SiC			2	N/C = 0.5, nucleation, SiC condens. onto graphite
Cherchneff & Barker 1992 [33]	6	70	C,SiC, SiO_2	1000-6000	$0.1 - 10^{-8}$	1.1, 1.5, 3.5	solar abund., emphasis on PAHs; kinetics
Lodders & Fegley 1995 [34]	90	~2000	600	1000-2500	$10^{-2} - 10^{-11}$	solar to 10	N/C=solar to 13, cond. seq. of major elem., emphasis on trace elements
Sharp & Wasserburg 1995 [35]	20	162	54	1200-2000	$5 \times 10^{-4} - 5 \times 10^{-10}$	0.89 to 3.02	Cond. seq. of major elements, kinetics
Helling et al. 1996 [36]	5?	376	none		$10^{-4} - 10^{-13}$	1.1 to 7	PAH, polyynes, P-T model for C-star atm.

? indicates that parameter is not well specified or not available in reference.

392

Table 1 lists many of the subsequent thermodynamic studies of carbon-star atmospheric chemistry. In general, the evolution of thermodynamic models proceeded in parallel with advances in spectroscopic studies of carbon stars, and was greatly aided by the invention of mainframe and later of personal computers, the development of powerful algorithms for multicomponent chemical equilibrium calculations, and by compilation of thermodynamic databases that include many species of interest in stellar atmospheres. More recently, the discovery of circumstellar grains in meteorites provided impetus for improved thermodynamic modeling of major and trace element chemistry in carbon star atmospheres.

Rosenfeld in 1933 [6,7] and Russell in 1934 [9] independently made thermodynamic calculations of gas chemistry in carbon stars, and it became clear that the increased C/O ratio favored increased abundances of carbon-bearing molecules suspected to be responsible for the violet depression in carbon stars. In the 1960s and 1970s, Tsuji [15,23] performed extensive calculations for gas chemistry of major and trace elements. His work is still an important reference for molecular speciation in carbon stars. More recent advances in thermochemical equilibrium calculations include consideration of large numbers of potential condensates, trace element solid solution formation, and inclusion of complex organic molecules, such as polycyclic aromatic hydrocarbons (PAHs) or polyynes [31,33,34,36].

The spectral classification of carbon stars has been debated since the early spectroscopic studies. Neither the R and N classification nor the C classification (based on the C_2 band strength and temperature) introduced by Keenan and Morgan 1941[37], and further developed by Yamashita in the 1970s [38,39], represent a good description of the spectra. The latest revisions in carbon star classification schemes can be found in Keenan 1993 [40] and Barnbaum et al. 1996 [41].

It is now apparent that the N and R stars do not form a continuous series and that these stars belong to different stellar populations [40]. Table 2 lists mean photospheric temperatures, abundances of some elements on the astrophysical atomic scale (log $N(H)$ = εH = 12.0), C/O and carbon isotope ratios for M, S, C-R and C-N stars, for another small group of cool, ^{13}C-rich "C-J" stars, and for reference, the solar data. Of particular interest here are the differences in effective temperature and chemical composition of the carbon stars.

For example, the C-R stars are hotter than the C-N stars. The C-N stars also show higher abundances of s-process elements such as Zr, Sr, and Ba (see Figure 1). The overabundance of Ba in C-N stars was detected as early as 1920 by Shane [42]. More recent work by Kilston [43], Utsumi [44,45] and Dominy [45,46] showed that s-process element abundances (e.g., Y, Zr, Sr, Ba, rare earth elements (REE)) reach 10-100 times solar values in C-N stars, while these abundances are basically solar in C-R stars. The ongoing s-process in C-N stars is also reflected by the presence of Tc in most of their spectra (e.g., [47]).

This is a similar situation as observed in M and S stars. The S-stars (C/O > solar to ~1) show ZrO bands that are stronger than the TiO bands, indicating s-

process element enrichments, while M-stars generally have abundances close to solar and relatively weak or no ZrO bands. The increased Zr abundances in S stars were already suspected by Wildt in 1929 [5]. The later thermodynamic modeling by Bouigue 1957 [10] and Cowley 1962 [12] showed the need for increased Zr, Sr, and Ba abundances in C-N stars. However, as discussed below, a uniform s-process enrichment in C-N star abundance patterns (Figure 1) is only one possibility. Fractionated elemental abundance patterns for C-N stars are also observed and may be caused by fractional condensation of trace elements into grains.

TABLE 2. Properties of Cool Stars Compared to the Sun

	M	S	C-N	C-J	C-R	Sun (G2V)
T_{eff} (K)	3500±100	3530±120	2650±250	2650±250	4600±200	5780
εC	8.52	8.55	8.75	8.72	9.08	8.55
εN	8.28	8.77	7.78	7.78	8.64	7.97
εO	8.86	8.75	8.71	8.62	8.86	8.87
εFe	7.37	7.36	7.53	7.58	7.4	7.51
s-process elements/solar	1	~ 10	10 - 100	1	1 - 2	= 1
Char. Bands	TiO (VO)	ZrO (LaO)	------------ C₂ CN CH ------------			Ca, Fe
Tc present	few	several	several	no	no	no
C/O	0.45	0.6 - 1	1.14±0.12	1.15±0.15	1.66	0.48
^{12}C/^{13}C	13±4	22±14	30 - 80	3 - 5	7±4	89
11.3 μm SiC em.	no	no	yes	yes	few	N/A
7.5/23 μm am. C emission	no	no	some	?	?	N/A
9.7 μm silicate emission	yes	yes	no	some	?	N/A
dM/dt (M⊙/yr)	10^{-7}- 10^{-5}	10^{-7}	5×10^{-8}-3×10^{-6}	10^{-8} - 10^{-7}	?	10^{-14}

Sources: [43-53]. N/A = not applicable.
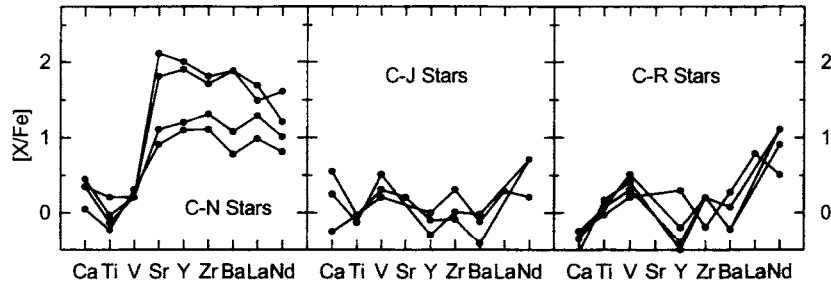
Figure 1. Elemental abundances in C-N, C-R, and C-J stars normalized to solar abundances [54] and Fe. The notation is: [X/Fe] = log (X/Fe)star - log (X/Fe)solar. The enhanced abundances of s-process elements in C-N stars are clearly visible. The uncertainties are about 0.5 dex (with those for REE probably larger), which is reflected in the scatter of the C-J and C-R data sets. All data from Utsumi [44].

The C-R stars have ^{13}C enrichments close to the CNO equilibrium value of ^{12}C/[13]C = 3.5, while the respective ratios in C-N stars range from 30-80 and are closer to the solar value (~89). The s-process element abundances and the ^{12}C/^{13}C ratios of the small group of C-J stars are comparable with those of the C-R stars. However, C-J stars have lower effective temperatures and somewhat smaller C/O ratios than C-R stars, and these properties are closer to those found for C-N stars.

The IRC two micron sky survey [55] and the observations from the Infrared Astronomical Satellite (IRAS) [56] revealed that a large fraction of the late type C-N and C-J stars radiate more strongly in the infrared than expected. The infrared excess is generally explained by thermal radiation from dust particles, which condensed and produced a circumstellar envelope (CSE). Earlier, Rosen & Swings 1953 [57,58] had suggested that solid carbon particles around a star could be responsible for the strong violet opacity in late N-type carbon stars.

In 1929, Wildt [5] concluded 'Kondensation scheint selbst in den kühlsten Sternatmosphären nicht einzutreten[2] but later in 1933, Wildt [8] explored condensation in reduced stellar atmospheres and predicted reduced condensates such as C and possibly SiC. Guided by the high melting points and high stabilities of refractory compounds, Wildt suggested that carbides and nitrides of Ti, Zr, Sc, and V may be the first condensates to form in N-star atmospheres. A thorough investigation of graphite condensation, grain formation times, and grain sizes was done in 1962 by Hoyle & Wickramasinghe [13]. Their paper includes several key conclusions that were rediscovered later by other authors. Wildt's 1933 prediction of SiC condensation in carbon stars was apparently forgotten. Over 35 years later in 1969, Friedemann [21] and Gilman [22] independently predicted SiC condensation in carbon stars. Friedemann also studied SiC formation timescales. Gilman's paper was the first work after Wildt in 1933 to include condensates other than graphite and to study the effect of C/O ratio on types of condensates in cool stars. Most modeling of carbon star chemistry did not include any condensates, or only C and SiC condensation (Table 1). Although not applied to carbon stars, Larimer 1975, Larimer & Bartholomay 1979 [59,60], and Lattimer et al. 1978 [61] also calculated major element gas chemistry and condensation for C/O ratios > unity.

The emission of radiation by dust in CSE prevents visual observations of some carbon stars, and several carbon stars were only detected by the IRC or IRAS surveys. Gilra 1972 [62] suggested that SiC dust produces the 11.3 μm emission band and Forrest et al. 1975 [63] concluded that excess IR emission at 8-14 μm in carbon stars is probably due to SiC grains. Since then, the 11.3 μm SiC dust emission has been used to classify carbon stars (e.g., [56,64]), while the 9.7 μm silicate emission has been used to characterize cool oxygen-rich stars. Both SiC and silicate emission is detected in several C-J stars. The reason for this dual emission is still under investigation (e.g., [65-67]).

---

[2] Condensation does not appear to occur in even the coolest stellar atmospheres.

The number of carbon stars is small, but their contribution of reduced dust to the interstellar medium (ISM) is significant. Thronson *et al.* [68] estimate that carbon stars provide 10-50% of the 0.35 $M_\odot$/yr of dust contributed by AGB stars to the ISM. Epchtein *et al.* [69] suggest an even higher dust contribution of 0.5 $M_\odot$/yr from infrared carbon stars alone. The presence of C or SiC dust in the ISM is not yet observationally established; only silicates have been identified [70,71]. Carbonaceous dust may have subsequently become coated by oxide layers or ice in the ISM so that detection of the SiC absorption is prevented [71]. Nevertheless, graphite and SiC grains should be present in the ISM because they are observed in stellar outflows and they were certainly present in the cloud of gas and dust which formed the solar nebula, as the meteoritic evidence shows.

Modern laboratory techniques allow the isolation of 0.8-7 μm sized graphite and 0.2-10 μm sized SiC grains from meteorites for detailed chemical, isotopic and structural analyses (see review by Anders & Zinner 1993 [72]). The isotopic compositions of these refractory grains clearly point to their presolar origin with a larger fraction of them most likely originating in N-star atmospheres, as discussed by Gallino and coworkers in the early 1990s [73,74]. These grains found their way into the gas and dust cloud which eventually collapsed to form our solar system and survived subsequent heating and condensation processes in the solar nebula before they became incorporated into meteorite parent bodies.

The laboratory investigations by Bernatowicz and coworkers [75,76] reveal that other refractory grains such as TiC and (Zr,Mo)C are present in the SiC and graphite grains. Thus, by implication, these trace element carbides must also be present in stellar atmospheres, but their direct observation is hindered by the relatively low abundances of Ti, Zr or Mo. The analyses of trace elements (such as V, Sr, Y, Zr, Ba, REE) in SiC grains by Amari *et al.* [77] also showed that trace elements are incorporated to different extents in SiC. The possibility of pure major and trace element compound condensation and solid solution formation of trace elements with preexisting condensates was explored from 1982 onward by Fegley and Lodders (summarized in [34]). The next sections describe some results of these calculations. The condensation calculations pinpoint the types of carbon stars responsible for presolar carbonaceous grains found in meteorites and provide information complementary to that from isotopic studies.

THERMODYNAMIC EQUILIBRIUM CALCULATIONS

In this section we describe our thermochemical equilibrium calculations together with some results reported in the literature. We focus the discussion on condensates and present a description of gas phase chemistry elsewhere. The next section illustrates the computational procedure using corundum (Al_2O_3) and Fe metal condensation as examples. Readers familiar with thermochemical

equilibrium calculations may want to skip to the section "Applicability of thermo-chemical equilibrium to stellar atmospheres".

Computational procedures

The condensation of Al, Fe, or another element in a stellar atmosphere is determined by several factors: the total pressure, the elemental abundances which determine the partial pressures in the gas, the distribution of an element between different gases and condensates, and the vapor pressure of the element. We use a computer program (CONDOR) to do the necessary calculations involved in considering these factors. The code operates by simultaneously solving for mass balance and chemical equilibrium for 2000 gaseous and 600 condensates of all naturally occurring elements [34,78,79].

In the case of Al, the total abundance of Al in all forms is $A(Al)$, which is the solar or stellar abundance of Al. The total mole fraction (X) of Al is then:

$$X_{\Sigma Al} = A(Al)/(A(H+H_2+He)) \qquad (1)$$

where $A(H+H_2+He)$ is the sum of the H and He solar or stellar abundances with the temperature dependent H and H_2 equilibrium taken into account. In the actual computation, other gases such as CO, H_2O, N_2, Ne, ions, etc. are also included in the denominator, but neglected in the description here for clarity.

Multiplying $X_{\Sigma Al}$ by the total pressure P_T gives the pressure of Al in all forms, which is equal to the partial pressure sum for Al :

$$P_{\Sigma Al} = X_{\Sigma Al}P_T = P_{Al} + P_{AlO} + P_{AlOH} + ... \qquad (2)$$

Equation (2) can be rewritten in terms of the thermodynamic activity of Al (a_{Al}), the equilibrium constants (K_i) for forming the Al gases from the constituent elements in their reference states, and the thermodynamic activities and fugacities of other elements combined with Al in gases:

$$P_{\Sigma Al} = X_{\Sigma Al}P_T = a_{Al}\left[K_{Al} + K_{AlO}f_{O_2}^{0.5} + K_{AlOH}f_{O_2}^{0.5}f_{H_2}^{0.5} + ...\right] \qquad (3)$$

The actual mass balance sum for Al in the CONDOR code includes 58 Al-bearing gases. The four most important ones in a solar composition gas are Al, AlO, AlOH, and AlH while in a reduced gas, only Al and AlH are important.

Analogous forms of equation (3) are written for each element in the code. The equilibrium constants (K_i) in the equations are taken from thermodynamic data compilations such as the JANAF Tables. The compounds in the CONDOR code and the thermodynamic data sources used are listed in [34,78,79].

397

As evident from equation (3), the chemistry of different elements is coupled. The mass balance equations form a set of coupled, nonlinear equations which are solved iteratively. An initial guess is assumed for the activity or fugacity of each element. These guesses can be optimized if the major gas for each element is known but this is not necessary for the code to operate properly. CONDOR solves the set of mass balance equations and gives the thermodynamic activity or fugacity for each element, the abundances of all gases (molecules, radicals, atoms, ions) included in the code, and information on the quality of the calculated results for each element. The convergence criterion requires that the calculated and input abundances for each element agree to within 1 part in 100,000 or better.

Stabilities of condensates are computed considering compound formation from the elements in their respective reference states. For example, the reaction:

$$2 \text{ Al (g)} + 1.5 \text{ O}_2 = \text{Al}_2\text{O}_3 \text{ (s)} \tag{4}$$
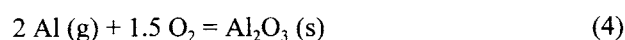
is used for corundum. Condensation occurs when the thermodynamic activity of Al_2O_3 reaches unity and this is calculated from:

$$a_{Al_2O_3} = a_{Al}^2 f_{O_2}^{1.5} K_{Al_2O_3} \tag{5}$$

where K_{Al2O3} is the temperature dependent equilibrium constant for corundum and a_{Al} and f_{O2} are taken from the gas phase equilibrium calculations described above. The stabilities of all 600 possible condensates are computed in a similar fashion.

Once corundum condenses, the fraction of Al (α_{Al}) in corundum is calculated and the gas phase abundance of Al ($P_{\Sigma Al}$) is reduced by multiplying by ($1-\alpha_{Al}$). Analogous corrections are made for all elements distributed between the gas and condensates. The gas phase and gas-solid chemical equilibrium calculations are coupled and are done simultaneously using iterative techniques.

Equations (3) and (4) show that the Al chemistry is affected by the oxygen fugacity, which in turn depends on the distribution of oxygen between CO, H_2O, SiO, and other O-bearing gases. The mass-balance sum for oxygen is:

$$P_{\Sigma O} = X_{\Sigma O} P_T = 2 f_{O_2} + f_{O_2}^{0.5} [K_{CO} a_C + K_{H_2O} f_{H_2} + K_{SiO} a_{Si} + ...] \tag{6}$$

where a_C and a_{Si} are the thermodynamic activities of carbon and silicon. Because the solar O/C and O/Si atomic ratios are ~ 2 and ~ 24, respectively, SiO is less important than CO and H_2O for controlling the fO_2. As the C/O ratio increases the CO/H_2O ratio increases and fO_2 decreases. Eventually AlN becomes the initial Al-bearing condensate instead of Al_2O_3 (see section 'Major condensates').

The chemistry of other elements, such as Ti, Zr, La, or Ce, also changes as the C/O ratio increases and fO_2 decreases. In the case of Ti, two important Ti gases are Ti and TiO, and the Ti mass balance sum is:

398

$$P_{\sum Ti} = X_{\sum Ti} P_T = a_{Ti}[K_{Ti} + K_{TiO}f_{O_2}^{0.5} + ...] \qquad (7)$$

As fO_2 drops, $K_{Ti} \gg K_{TiO}(fO_2)^{0.5}$ and the TiO (g) abundance also drops. This chemistry is reflected by the disappearance of TiO bands as we go from M-stars (C/O ~ 0.45) to carbon stars (C/O ≥ 1, see Table 2).

For some elements, the gas chemistry is independent of C/O ratio. This is particularly true for the Fe and Ni-group metals in the periodic table. For example, monatomic Fe gas is the dominant Fe species at any given C/O ratio. The condensation reaction is:
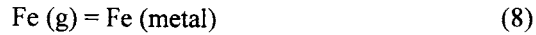
$$\text{Fe (g)} = \text{Fe (metal)} \qquad (8)$$

for which the equilibrium constant is:

$$\log (K_{Fe}) = \log (a_{Fe}/P_{Fe}) = A + B/T \qquad (9)$$

and the condensation temperature follows from:

$$a_{Fe} = 1 = K_{Fe} P_{Fe} \quad \text{so that} \quad -\log P_{Fe} = A + B/T \qquad (10)$$

The reverse of reaction (8) is nothing else than the evaporation reaction of Fe metal to Fe (g), for which we can write the vapor pressure equation $\log P_{vap} = A'+B'/T$ with A' = -A and B' = -B. Therefore, the equilibrium condensation temperature is the temperature where the gas partial pressure (P_i) equals the vapor pressure (P_{vap}) of the condensing species. In other words, the saturation ratio S = $P_i/P_{vap} = 1$ equals the thermodynamic activity a_i.

Applicability of thermochemical equilibrium to stellar atmospheres

As discussed below, pressures in stellar atmospheres are typically smaller than 10^{-3} bars and we have to ask if thermochemical equilibrium applies. The success of thermochemical equilibrium calculations in reproducing the relative abundances of various species observed in stellar atmospheres shows that equilibrium applies for gas near the photosphere where sufficiently high pressures and temperatures are present (see also Tsuji [15,23]). As gas travels outwards from the photospheric region, gas outflow time scales become small relative to chemical reaction times, and chemical equilibrium is not reached in the low pressure and temperature regions in the outer CSE. Instead, thermochemical equilibria become frozen in at different distances and photochemistry determines the chemical changes occurring in the gas (see Glassgold [80]).

If gases equilibrate in regions near the photosphere, we may expect that gas-solid equilibria also occur. However, a large body of work implies that ideal condensation (i.e., S = 1) does not occur, but that the gas has to be supersaturated for

condensates to nucleate. We find that calculations using S = 1 satisfactorily repro-
duce the observed locations of dust in CSE and that the calculated condensation
sequence agrees with laboratory studies of presolar grains. We also discuss some
aspects of supersaturation for graphite condensation.

The next sections give the necessary physical and chemical input parameters
for the calculations related to carbon star CSE. We then present results for major
element condensates, followed by SiC trace element abundance pattern modeling.

Chemical and Physical Input Parameters in the Calculations

The bulk elemental abundances, and pressure (P) - temperature (T) conditions
in carbon star atmospheres are needed for the condensation calculations. Much
progress has been made in determining these properties. However, there is one
particular property of carbon stars, namely stellar variability, which complicates
the modeling. Most carbon stars belong to the group of pulsating variable stars,
which are stars with periodic changes in brightness.

The discovery of stellar variability dates to August 12, 1596, when pastor
David Fabricius in Ostfriesland, Northern Germany, began observing a star in the
constellation Cetus (sea monster). Initially a red star of second magnitude, the star
began to fade and eventually disappeared in October of the same year (note that at
this time telescopes were not yet invented). It took until February 1609 for Fabri-
cius to find the star again, which had miraculously returned[3]. This star, subse-
quently named o Ceti and Mira (the wonderful), has become the prototype of long
period variable stars. Most of the carbon stars fall within three groups of variable
stars: (1) Mira variables with well expressed variability and periods from 80-1000
days, (2) SR variables, semi regular variables with well defined periods from
50-300 days with appreciable irregularities, and (3) Lb variables, which are ir-
regular pulsating variables (see *Catalogue of variable stars* [100]).

In the last century, Secchi had already noted that stellar variability is a typical
property of many carbon stars, but variability is still often neglected in gas and
dust thermochemical modeling. The brightness (and thus T, and radius R) vari-
ability is unfortunately also often neglected when temperature and photospheric
radius determinations of carbon stars are made. Apparent discrepancies between
different T and R measurements may arise from this neglect. Variability causes
problems in determining representative T, P, and R variations, which are neces-
sary inputs for thermochemical modeling. The elemental abundance determina-
tions may become affected by variability as pointed out by Russell in 1933 [9].
Locations of dust forming regions in stellar atmospheres are often referenced to
the photospheric radius; however, if the photospheric radius changes as a function

---

[3] Historical accounts of the discovery circumstances can be found in F. Plassmann, *Him-
melskunde*, 1898, Herdersche Verlagshandlung.

of time it is a poor reference point. Similarly, the effective temperatures listed in Table 2 are mean temperatures of several carbon stars, and for each individual star the photospheric temperature must be understood as an average temperature between minimum or maximum phase.

Temperatures and Pressures

The periodic changes in luminosities, effective temperatures and photospheric radii of the regular pulsating carbon miras are the best documented cases; we are not aware of similar studies involving semi regular (SR) or irregular (Lb) pulsating carbon variables. Miras have their highest effective temperatures and their lowest photospheric radii at maximum light. For example, Bergeat & Sibai [81] show that U Cyg (P=463 days) has T_{eff} ~2300 K and R_{ph} ~140 $R_\odot$ at maximum light while T_{eff} drops to ~1800 K and R_{ph} increases to ~360 $R_\odot$ at minimum light (assuming a distance of 230 pc for U Cyg). Thus, at minimum light temperatures drop significantly and dust formation becomes more efficient. The periodic changes in T and R also must affect the atmosphere, so the dust formation distance from the central star must vary as a function of the light curve. As photospheric temperatures drop from maximum to minimum, temperatures farther away from the photosphere change correspondingly, allowing more grain condensation during minimum phase. A detailed model of grain condensation as a function of light phase for the carbon mira R For is described by LeBertre [82]. He notes that the equilibrium temperature at a given distance from the central star changes with phase and that grains condense between maximum and minimum while grains are depleted by evaporation between minimum and maximum. However, evaporation of grains may not occur if grains are expelled from the hotter regions of the CSE. Radiation pressure can accelerate the grains and push them to outer regions of the CSE and beyond, as shown by the numerical models of Gail and Sedlmayr [83,84]. Radiation pressure-induced dust-driven winds and expulsion of dust from CSE are generally very important for understanding mass loss mechanisms from carbon stars (see reviews by Lafon & Berruyer [85], Danchi & Bester [86]).

The efficiency of grain removal from the CSE depends on the time required for a grain to travel into cooler regions *vs.* the time available between minimum (enhanced grain condensation) and maximum (enhanced grain evaporation). As shown by Olofsson [52,53], mass-loss rates increase with variability period and apparently with expansion velocities. However, there is no clear trend of mass-loss rate with effective temperature. We fitted the mass-loss rates for N-stars to the equations:

$$dM/dt \ (M_\odot/yr) = -(1.36\pm0.63)\times10^{-6} + (7.23\pm1.71)\times10^{-9} \ P \ \text{(days)} \qquad (11)$$

$$dM/dt \ (M_\odot/yr) = -(0.90\pm0.55)\times10^{-6} + (1.43\pm0.41)\times10^{-7} \ v_{exp} \ (km/s) \qquad (12)$$

If grain formation is responsible for accelerating the gas and for initiating mass-loss, grain production and survival is most favorable in long period (LP) variable stars. Typical values for LP variables are P ~300 d and v_{exp}= 15 km/s. The distance a grain has to travel between minimum and maximum to escape is Δr ~ $v_{exp}\times P/2$. Taking the data for U Cyg, (P = 463 days, v_{exp} = 14.2 km/s) we see that between minimum and maximum Δr ~ 400 $R_\odot$. This distance needs to be compared to the location of the grain evaporation front in the stellar atmosphere at maximum light. If no gas and dust acceleration occurred, dust formed at minimum would fall back into hotter regions and could evaporate during maximum phase. However, as the dust travels outward, the distance to the evaporation front is increased by Δr. As a result, the dust may never fall back to the grain evaporation front. In the example above for U Cyg, the difference in photospheric radii between maximum and minimum is 220 $R_\odot$. This is smaller than the distance Δr ~ 400 $R_\odot$ a dust grain can travel outwards and thus grains can survive.

For our calculations we use the model atmospheres for C-stars from Jorgensen *et al.* [87]. They give P-T grids for carbon stars as function of effective temperatures (2500-3100 K), gravities (log g -0.5 to 0.5), and stellar masses (0.7-100 $M_\odot$). We use their P-T data and assume a hypothetical 3 $M_\odot$ star with T_{eff} = 2800 K and log g = 0.5 at maximum and T_{eff}= 2500 K and log g = -0.5 at minimum.
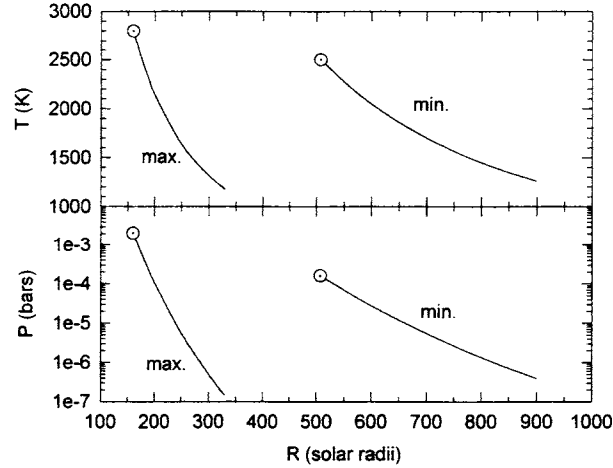
Figure 2. Temperature and pressure distribution in the atmosphere as a function of distance from the central star. Shown are curves for a hypothetical 3 $M_\odot$ star with T_{ph} = 2800 K, R_{ph} = 160 $R_\odot$ at maximum phase and T_{ph} = 2500 K, R_{ph} = 510 $R_\odot$ at minimum phase. Photospheric data are indicated by the dotted symbols. The P and T data are taken from [87] and are related to R by an adiabatic T-R distribution. See text for details.

The P-T grids of Jorgensen *et al.* are given for temperature ranges of ~1500-2200 K, which are in the range where condensation is expected to occur. If necessary, we extrapolated these P-T data. We calculate grain condensation as a function of radial distance (R) from the star and assume that T_{eff} values reflect photospheric temperatures, to obtain T and P as a function of R. The photospheric radius is obtained from $g = GM/R^2$ as 160 $R_\odot$ at maximum and 510 $R_\odot$ at minimum. With these photospheric T and R values, we calculate an adiabatic temperature distribution from:

$$T(R) = T_{ph}(\frac{R_{ph}}{R})^{3(\gamma-1)} \tag{13}$$

where γ is the adiabat coefficient ($\gamma=C_p/C_v$) taken here as 7/5. The T-R relation is shown for maximum and minimum light phases in the top of Figure 2. The plot of pressure *vs.* radial distance at the bottom of Figure 2 is calculated from the P-T and T-R relationships. In our calculations we use either the P-T profiles shown in Figure 2 or a constant total pressure of 10^{-5} bars.
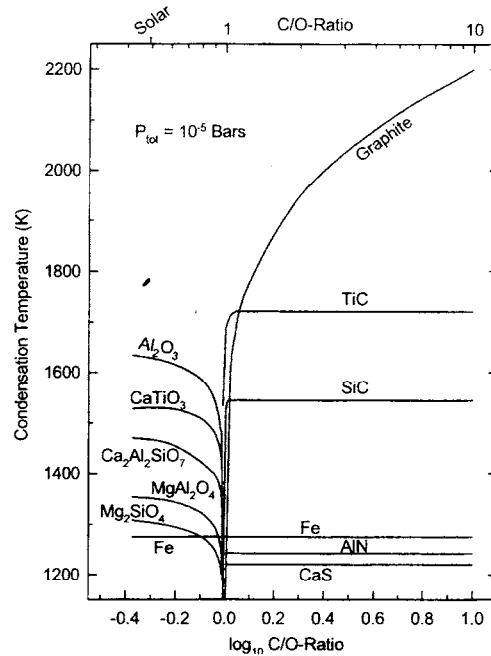
Elemental Abundances

The data in Table 2 show that major element (i.e., CNO) abundances in carbon stars are essentially solar except for carbon, which is enriched so that C/O $\geq$ 1. We therefore use the solar abundance data of Grevesse & Noels 1993 [88], who revised the CNO, Fe, Ti, and some other elemental abundances listed by Anders & Grevesse 1989 [54]. In our calculations we systematically increase the carbon abundance to obtain C/O ratios from solar to four. In some cases we substitute the solar CNO and Fe abundances with the mean data for C-N stars from Lambert *et al.* ([51], see Table 2) to better approximate "real" carbon star compositions. We also increased the abundances of s-process elements by up to a factor of ten, since s-process elemental enhancements of this magnitude are typical for C-N stars.

Major Element Condensation

The increased C/O ratio in carbon stars leads to different gases and condensates than those occurring in environments with C/O < 1, such as normal M-stars or our solar nebula. The different types of condensates as a function of C/O ratio (for constant total P = 10^{-5} bars) are illustrated in Figure 3, which was calculated by increasing the carbon abundance.

Oxides and silicates dominate at C/O < 0.98 and carbides, nitrides and sulfides appear at C/O $\geq$ 0.98 [60,61,34]. Note that condensation temperatures may vary if the C/O ratio is increased by removing oxygen instead of adding carbon (see Lodders & Fegley 1993 [78]). However, carbon dredge-up is the most likely mechanism for increasing the C/O ratio in carbon stars.

FIGURE 3. Condensation temperatures of major element condensates as a function of C/O ratio. Solar abundances [54,88] are used and the carbon abundance was increased from the solar value. At the solar C/O ratio (0.48) oxides and silicates are primary condensates. Hibonite ($CaAl_{12}O_{19}$) condensation temperatures are close to those of corundum (Al_2O_3) and are not plotted. An increase in C/O ratio from solar reduces the condensation temperatures of oxides and silicates because more oxygen is consumed by CO. At C/O > 0.98, reduced condensates appear. MgS (not shown) condenses below CaS at ~ 1020 K. The Fe-metal condensation temperature is independent of C/O ratio. At C/O > 1 the Fe_3C condensation temperature coincides with that of Fe metal.

The condensation sequence of reduced condensates is sensitive to the C/O ratio. This is illustrated in Figure 4, which also shows the P dependence of the condensation sequence for TiC, carbon, and SiC. At any given P and C/O ratio, TiC always condenses prior to SiC. Low C/O ratios from 1-1.2 (which are observed for N-type stars [51]) and relatively high pressures (log P > ~ -4) yield the sequence TiC-SiC-C, while at lower P (-6 < log P < -4) the sequence is TiC-C-SiC. The latter sequence seems to be recorded in circumstellar graphite grains from the Murchison meteorite. Bernatowicz *et al.* 1996 [76] found TiC grains embedded at or near the center of the graphite grains and TiC probably served as nucleation sites for graphite. Among the 67 graphite grains studied, Bernatowicz *et al.* found only one where a SiC grain was present in the graphite implying that the majority of graphite grains formed at intermediate P (Figure 4), if C/O ratios of 1-1.2 are representative for stars where the graphite grains originated. The last condensation

sequence in Figure 4 (C-TiC-SiC) is for relatively low pressures (log P ~ <-6). Such low pressures are apparently uncommon in grain-forming regions of C-stars because graphite grains embedded in TiC grains are not observed (see also [76]).
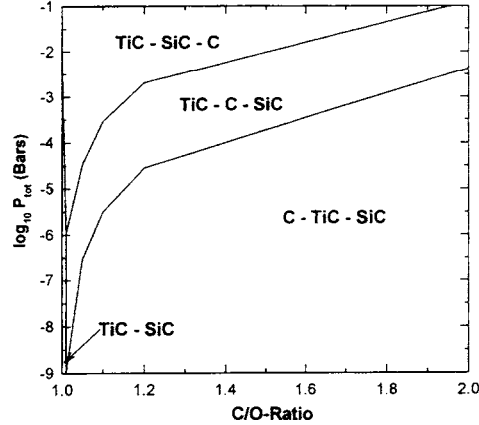

FIGURE 4. The condensation sequence of TiC, carbon, and SiC as a function of C/O ratio and total pressure. Data from [34].

The condensation sequence of TiC, graphite, and SiC is also found along the P-T profiles shown for maximum and minimum phase (Figure 2). Using typical N-star abundances (Table 2, [51]), we find condensation temperatures of 1705 K (TiC), 1645 K (graphite), 1486 K (SiC) at maximum and 1688 K (TiC), 1644 K (graphite), 1481 K (SiC) at minimum light. The similarity of condensation temperatures at maximum and minimum light is due to the very similar P-T profiles, however, the radial distances at which the condensates appear are different at maximum (~220 $R_\odot$) and minimum (~720 $R_\odot$).

The condensation temperatures for graphite, TiC, SiC, and for refractory Zr and Mo carbides are illustrated as a function of total pressure in Figure 5. Several curves at different C/O ratios are drawn for each condensate. This graph and Figure 3 illustrate that graphite condensation temperatures vary strongly with both C/O ratio and total P whereas carbide condensation temperatures are relatively independent of C/O ratio and essentially are only pressure dependent.

Once the temperature drops, graphite starts forming and carbon is removed from the gas thus lowering the C/O ratio in the gas. For all four bulk C/O ratios indicated in Figure 6 the C/O ratio of the gas reaches unity at ~1400 K. Graphite condensation fixes the partial pressures of carbon bearing gases and the SiC condensation temperature (e.g., 1544 K at P = 10^{-5} bars) becomes independent of the C/O ratio. As shown in Figure 3, SiC condensation temperatures are independent of the bulk C/O ratio at low pressures where SiC condenses after graphite. The explanation for this is given in Figure 6, which shows the C/O ratio in the gas phase

as a function of temperature. At high temperatures all carbon is in the gas and the C/O ratio of the gas is the same as the bulk C/O ratio.
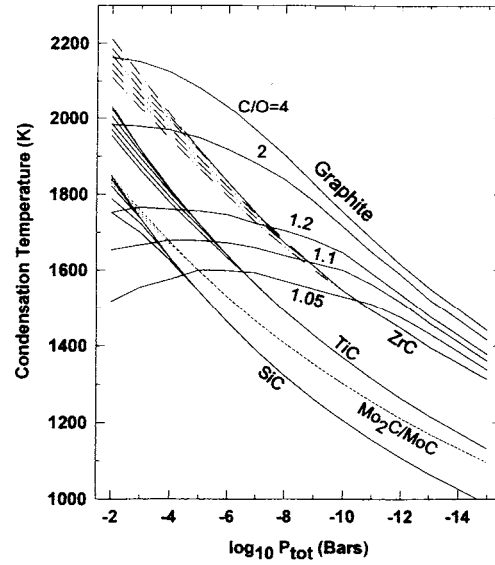
FIGURE 5. Dependence of condensation temperatures on total pressure. The numbers along the graphite condensation curves indicate the C/O ratio.
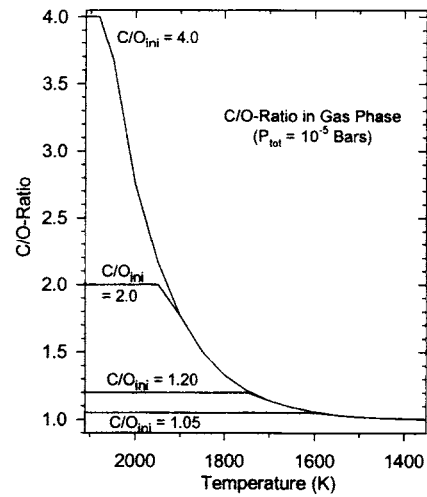
FIGURE 6. The effect of graphite condensation on the C/O ratio in the gas phase illustrated for four bulk C/O ratios (1.05, 1.2, 2, & 4). At high T, all carbon is in the gas phase. Graphite condensation removes carbon from the gas and the C/O ratio of the gas approaches unity.

At this point, we briefly want to address the effects of supersaturation on graphite condensation. Thermodynamically, condensation occurs when the activity of graphite becomes unity, that is, the saturation ratio equals unity. Precipitation of graphite from the gas may, however, be delayed and require higher C partial pressures before nucleation sets in. This is particularly true if no nucleation seeds are present and homogeneous nucleation is required. Carbon nucleation has been addressed by several authors but the results are still inconclusive.

In 1933, Wildt [8] proposed that ions in stellar atmospheres may serve as nucleation seeds. Using classical nucleation theory, Donn *et al.* 1968 [19] found that carbon supersaturation ratios of ~2.2 are sufficient for graphite precipitation on preexisting ions, yielding particle sizes ~0.05 μm. Using similar nucleation constraints Fix 1969 [20] finds that ionic nucleation in mira variables would yield extremely small ($\sim 5 \times 10^{-4}$ μm) carbon particles. Kamijo 1969 [89], Lucy 1974 [5] and Shmeld 1985 [32] concluded that homogeneous nucleation of graphite from gaseous carbon seems probable in reasonable timescales. However, uncertainties in particle surface energies and supersaturation ratios in stellar atmospheres led Tabak *et al.* 1975 [90] to conclude that there is no reliable answer about whether carbon nucleation takes place in cool carbon-rich stars.

Nevertheless, Salpeter 1974 [24] concluded that ionic nucleation as well as graphite formation from C (gas) is unimportant and he favors formation of carbon particles from hydrocarbon pyrolysis (i.e., C_2H_2). For over 30 years it has been known that C_2H_2 (and HCN) are the most abundant carbon bearing species after CO in C-rich atmospheres at lower temperatures and higher pressures (e.g., Tsuji 1964, 1973 [15,23], Lewis & Ney [27]). Sharp & Wasserburg 1995 [35] recently discussed this point. All carbon that is not in CO resides mainly in C_2H_2 and is often referred to as "excess carbon" or "condensible" carbon. The carbon condensation reaction is then $C_2H_2 = 2$ C(s) + H_2, implying that C_2H_2 breakdown plays an important step in carbon condensation. The possible importance of higher hydrocarbons and polycyclic aromatic hydrocarbons (PAH) for carbon condensation has now gained more attention. Calculations by Cherchneff & Barker 1992 [33] and Helling *et al.* 1996 [36] indicate that if carbon condensation is inhibited, significant PAH formation may occur at low temperatures (<1000 K). The PAHs then could serve as building blocks for amorphous carbon and graphite particles. Unfortunately, at temperatures where significant PAH formation is predicted, the PAH formation timescales are much longer than gas residence times in the stellar atmosphere. Thus, PAH induced carbon condensation may not occur [36].

If graphite condensation is kinetically inhibited, the gas-phase carbon chemistry must change to accommodate the "excess" carbon. Lewis and Ney 1979 [27] showed that hydrocarbon formation (C_2H_2, C_2H_4, CH_4) becomes more important at lower temperatures if graphite precipitation is inhibited. In the case of complete equilibrium, hydrocarbons are unimportant at low temperatures because carbon is removed from the gas by graphite condensation.

Figure 7 shows condensation temperatures of graphite as a function of C/O ratio for a total pressure of 10^{-5} bars. The top curve shows the equilibrium case (S=1). The bottom curve shows the graphite condensation temperatures for a supersaturation ratio of three, a typical value used in nucleation models (e.g., Lucy [25]). At C/O = 1.05, graphite condensation temperatures drop about 180 K when S is increased from one to three, while for C/O = 2 the temperature difference is about 260 K. Thus dust forms farther away from the star in a supersaturated gas. The equilibrium condensation temperature of graphite is 1645 K (~720 $R_\odot$) for the minimum P-T profile in Figure 2. Lowering the graphite condensation temperature ~200 K by supersaturating the gas to S = 3 leads to graphite formation at ~800 $R_\odot$. At larger supersaturation ratios of e.g., S ~ 30 graphite forms at ~970 $R_\odot$. We will see below that the observed dust-formation locations in CSE are compatible with equilibrium condensation temperatures and that supersaturation ratios are probably not significantly greater than unity.

We note that observations of CH_4 and measurements of the C_2H_2/HCN abundance ratio in carbon stars may constrain the graphite supersaturation ratio. Methane is expected to be more abundant in supersaturated C-bearing gas than in gas with low supersaturation ratios because the CH_4 abundance increases with decreasing temperature. A very sensitive test for strict equilibrium may be the ratio of C_2H_2/HCN, which should be below unity if graphite condensation takes place, while ratios above unity at temperatures where carbon condensation is possible indicate carbon supersaturated gases.
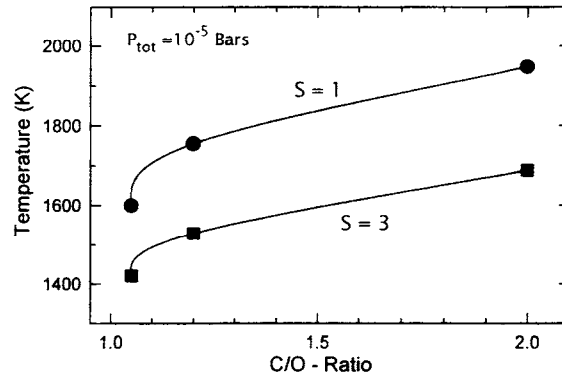
Figure 7. The thermodynamic equilibrium condensation temperatures of graphite are given at supersaturation ratio S=1 as a function of C/O ratio in the top curve. The bottom shows the temperatures for a supersaturation ratio of three.

Yet another important question is whether carbon condenses as crystalline graphite or in an amorphous form. For example, observational models for thick dusty CSE of the well known carbon stars IRC +10216 and CIT 6 often assume the presence of amorphous carbon particles (e.g., Martin & Rogers [91], Orofino

et al. [92,93]). The thermochemically stable carbon condensate is crystalline graphite but if nucleation is unfavorable, amorphous carbon may form instead. We use the thermodynamic properties of coke (a form of amorphous carbon) determined by Jacob & Seetharaman 1994 [94] to calculate condensation temperatures of amorphous carbon. The equilibrium condensation temperature of amorphous carbon is always lower than that of crystalline graphite in a C-rich, otherwise solar gas. The effect is most pronounced at higher total pressures. For example, for C/O=1.05 at P= 10^{-5} bars crystalline graphite condenses at 1600 K; if no graphite forms, amorphous carbon condenses 180 K lower at about 1420 K. At 10^{-11} bars total pressure, the difference in condensation temperatures decreases to 74 K, 1514 K for graphite and 1440 K for amorphous carbon. Higher bulk C/O ratios also decrease the gap between graphite and amorphous carbon condensation. At C/O = 2 and P=10^{-5} bars amorphous carbon condenses at 1840 K, which is about 110 K lower than the graphite condensation temperature.
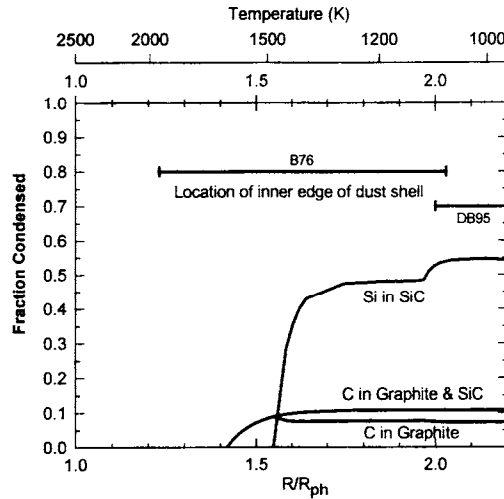
Figure 8. The fraction of total carbon or Si condensed in graphite and SiC as a function of temperature and radial distance. The P-T profile for minimum phase (R_{ph} = 510 $R_\odot$ from Figure 2 and N-star elemental abundances are used. The two horizontal bars indicate the position of the inner edge of the dust shell in the CSE as obtained from spectroscopic observations (B76 = [95], DB95 = [86]). Equilibrium condensation calculations indicate dust formation within the observed ranges of the inner dust shell. The increase in the amount of SiC condensed at 1100 K is due to CaS (s) condensation, which removes sulfur from the gas and releases Si from SiS (g) for further SiC condensation. See text for more details.

However, even if graphite condensation (at 1645 K) is replaced by amorphous carbon (at 1516 K) for the P-T profiles in Figure 2, the condensation sequence is still TiC, carbon, and SiC, in accordance with the observed condensation

sequence. In the graphite grains studied in the laboratory, TiC grains are often enclosed in amorphous carbon and the amorphous carbon becomes more graphitized towards the outside (Bernatowicz et al. [76]). Thus, amorphous carbon becomes replaced by graphite as condensation proceeds. Instead of referring to a specific condensation temperature for carbon it may be more useful to introduce a 'condensation temperature range', which is defined by the amorphous carbon and graphite condensation temperatures (e.g., 1516-1645 for the P-T profile in Figure 2).

The calculations also give information about the amount of C and SiC condensed as a function of temperature and pressure (or distance from the photosphere). Figure 8 shows the fraction of carbon condensed in graphite and SiC and the fraction of Si condensed in SiC as a function of decreasing temperature and increasing distance from the photosphere calculated with N-star abundances (C/O = 1.1; Table 2) and the minimum P-T profile from Figure 2. The photospheric radius at minimum is taken as a reference point for the distance from the central star. Condensation of graphite starts at ~ 1.42 R/R_{ph} and SiC at around 1.55 R/R_{ph}. At this low C/O ratio, the amount of carbon tied up in condensates is small; only about 10% of the bulk carbon is eventually in graphite and SiC. Initially SiC condensation removes ~45% of all Si from the gas until CaS forms. Condensation of CaS removes sulfur from the gas and releases Si (g) from SiS (g) so more SiC condenses. About 55% of all Si is finally bound in SiC.

Figure 8 also shows the location of the inner edge of the dust shell in the CSE from observations of Bergeat et al. [95] and Danchi & Bester [86]. Note that the position of these bars on the y-axis is arbitrary because the observations constrain R/R_{ph} but not the fraction condensed. The distances where equilibrium calculations predict that dust starts forming coincide with the two ranges where dust is observed in CSEs. Only small amounts of dust form at the condensation point. Larger amounts of dust form and become spectroscopically detectable at lower temperatures, that is, at larger distances. Although TiC is the first major condensate the Ti abundance is probably too low to allow detection of TiC dust in CSE.

If the bulk C/O ratio is higher than 1.1 (the C/O ratio used in Figure 8) graphite dust forms closer to the photosphere because graphite condensation temperatures increase with increasing C/O ratio. The fraction of carbon condensed as graphite will then also become proportionally larger than indicated in Figure 8.

Variability and C/O-Ratio

The condensation of graphite and SiC relatively close to the photosphere may also provide an important clue for interpreting the observed C/O ratios in N-type carbon stars. The average C/O ratio in 60 cool N-type carbon stars is 1.16 ± 0.14 [51,53], while the hotter R-type carbon stars have higher C/O-ratios of 2±1 [45]. We may ask why N-stars do not exhibit higher C/O ratios.

In Figure 8 we plotted the fraction of C and Si condensed as a function of distance from the photosphere for the minimum light phase. Although condensation temperatures at minimum and maximum are very similar, dust formation at minimum occurs at much greater distances from the central star. Temperatures at minimum may be even lower than in our examples and dust production in C-N stars could become more efficient. In contrast, the hot C-R stars (R0-R4) are nonvariable stars and their temperatures are too high to allow efficient graphite and SiC formation (if any). Although present, IR excesses in C-R stars are much less prominent, indicating the presence of only small amounts of dust.

On the other hand, in the colder N-type carbon stars, carbon bearing dust can form, preferentially during minimum phase in the variability cycle. Formation of graphite and SiC removes carbon from the gas and consequently lowers the C/O ratio in the gas, as illustrated in Figure 6. Fix 1969 [19] also illustrates the C/O ratio decreasing to unity during graphite condensation at minimum phase in the variability cycle. Fix notes that if the stellar atmosphere contracts again and the star moves into maximum phase, grains formed during the minimum phase may evaporate again and raise the C/O ratio of the gas back to the original value. However, if graphite and SiC are expelled by radiation pressure the gas remains with a C/O ratio close to unity (see discussion above).

If grain formation and expulsion preferentially occur during minimum, the carbon depleted gas falls back onto the photosphere during stellar contraction towards maximum. Therefore the C/O ratio in the gas eventually approaches unity, which is what is found from measurements of the C/O ratio from molecular lines in the *gas*. Upward mixing of carbon from the stellar interior can increase the photospheric C/O ratio but carbon condenses out as soon as temperatures drop sufficiently again. All determinations of C/O ratios in N-type carbon stars are done using the gas composition while the actual bulk stellar C/O ratio could be higher. Photospheric determinations of stellar C/O ratios may only be valid for stars without dust; if dust is present the bulk C/O ratio of the star must be computed from (Cgas + Cdust)/O. This is particularly important for the exceptional objects IRC +10 216 and CIT 6 which show carbon dust emission and have large amounts of dust in their CSE [91-93]. In these stars carbon-bearing dust condensation must have lowered the C/O ratio in the gas. On the other hand, for a bulk C/O ratio of 1.05, only about 10% of all carbon eventually condenses as graphite and SiC and the effect of carbon removal from the gas is not that prominent.

Trace Element Condensation

We now calculate trace element patterns in SiC as a function of temperature and compare these to observed abundance patterns in circumstellar grains isolated from the Murchison meteorite (Amari *et al.* [77]). These calculations have been previously described in detail [34] and are only briefly reviewed here.

In contrast to more abundant major elements, trace elements (Zr, Mo, V, Sr, Ba, REE) generally form solid solutions with preexisting condensates, such as TiC or SiC. The condensation of trace elements into TiC or SiC is governed by their volatility. Highly refractory elements (Zr, Mo) readily form solid solutions with TiC, as has been observed [76]. Silicon carbide forms at lower temperatures than TiC and if gas-solid equilibrium persists, TiC, and trace elements already condensed in it, can also dissolve in SiC.

Less refractory elements such as the REE, Sr, and Ba condense into SiC at lower temperatures. The two most volatile elements are Sr and Ba. Figure 9 shows calculated trace element abundance patterns in SiC as a function of decreasing temperature for the minimum P-T profile in Figure 2. We used N-star CNO abundances listed in Table 2 and ten times solar s-process elemental abundances for the calculations. We assume ideal solid solution behavior [34]. The abundance patterns in Figure 9 are normalized to CI-chondrites (essentially solar) and Si. Figure 8 shows that the amount of Si condensed is also a function of temperature and that only about 55% of all Si condenses as SiC. Thus, normalizing to Si introduces about a factor of two into the normalization in Figure 9. For example, if V is present in solar abundances in N-stars and fully condenses into SiC, the CI-chondrite and Si normalized abundance of V is ~2. Similarly, if s-process elements are 10 times more abundant in N-stars and fully condensed into SiC they plot at ~20 in Figure 9. SiC starts condensing at 1481 K, and at 1480 K only about 0.17% of all Si is condensed as SiC. Refractory carbides of Ti, V, Zr, Nb, Mo, and, to some extent Y, either form their own condensates or condense into solid solution with each other prior to SiC formation. Once SiC forms, these refractory carbides can be readily incorporated into SiC. Thus, the Si-normalized relative abundances of these refractory trace elements are very high (500-6000) at 1480 K (top graph in Figure 9) because they are fully condensed but only very little Si is condensed. Lanthanum, taken as representative for the refractory REE, condenses as LaS into SiC and is not as refractory as the carbides mentioned above. REE carbides or nitrides were also considered as potential candidates dissolving in SiC. However, the REE sulfides are generally more stable than carbides and nitrides (see also [34,78]. The strong depletions of Fe, Ca, Al, Sr, and Ba at 1480 K show that these elements are more volatile.

At 1380 and 1280 K, more Si (43% and 47%, respectively) is condensed in SiC, leading to a 'dilution' of the abundances of highly refractory elements so that their normalized abundances plot around 2-20. Still, at 1280 K less than one percent of the volatile elements Ba, Sr, or Ca are condensed and the amount of Al condensed as AlN into SiC (~ 0.7% of total Al) or Fe as Fe_3C (~ 2% of total Fe) is fairly small. Another 100 K temperature decrease allows more condensation of Fe, Ca, and Al into SiC and these elements could be fully incorporated into SiC by 1080 K. However, Fe, Ca, and Al may also form their own condensates instead of condensing into SiC. Iron metal or Fe_3C (1150 K for either), AlN (1120K), and

412

CaS (1100 K) condense relatively close to the temperature where ideal solid solution with SiC occurs. Thus, solid solution formation in SiC may compete with the formation of pure compounds of these elements. If CaS condensation occurs, the amount of Si condensed as SiC also increases as explained above for Figure 8.
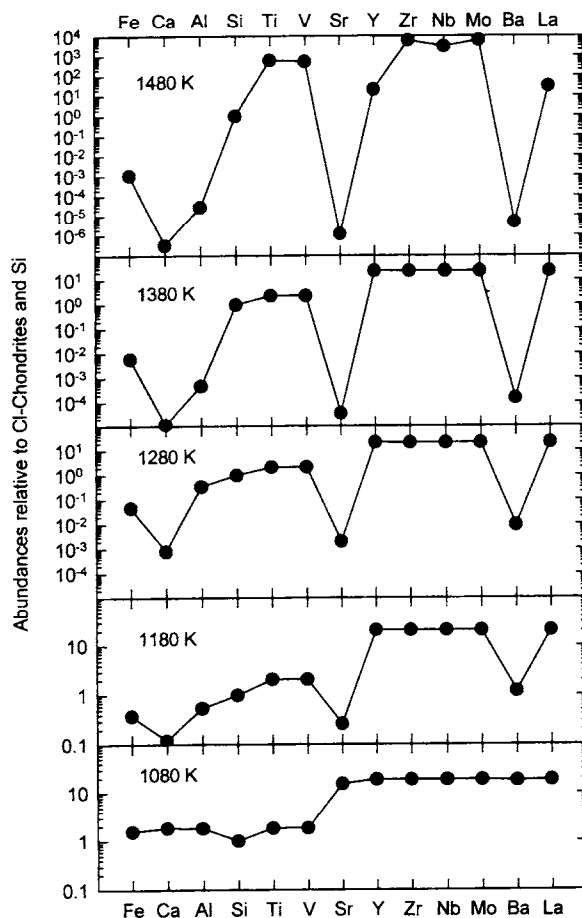
Figure 9. Calculated trace element abundances in SiC as a function of decreasing temperature for the minimum light P-T profile from Figure 2. The s-process element abundances are taken as ten times solar. SiC starts forming at 1481 K and at 1480 K, only 0.17% of all Si is condensed as SiC. Refractory carbides of Ti, V, Zr, Mo, and Nb condense prior to SiC and become readily incorporated into SiC so that their relative abundances are extremely high. Note the different abundance scales on the individual graphs. At 1380 K, about 43% of all Si is condensed and more of the relatively volatile Fe, Ca, Al, Sr, and Ba condense into SiC as the temperature drops. At 1080 K, about 54% of total Si is condensed as SiC and all trace elements are in SiC.

413

The other two volatile elements, Sr and Ba, are not abundant enough to form their own condensates and they are also the most volatile elements among those shown. At 1180 K, about 6% of all Ba and about 1.3% of all Sr are condensed into SiC. Note that Sr plots at about 20 if fully condensed, which is not the case by 1180 K. Only by 1080 K do we obtain the trace element abundance pattern showing all elements fully condensed into SiC. As mentioned before, CaS condenses at 1100 K and trace elements not condensed into SiC by that temperature may dissolve into CaS. The CaS condensation temperature is calculated assuming that no CaS is dissolved in SiC. However, as in Figure 9, at 1180 K the normalized abundance of Ca condensed into SiC is ~ 0.1, which indicates that about 20% Ca is already taken out of the gas. Thus, the condensation temperature for pure CaS becomes depressed and trace elements may continue to condense into SiC. We come back to Ca condensation later.

The trace element patterns obtained by fractional condensation are compared to measured abundance patterns in SiC grains isolated from meteorites. Amari et al. [77] determined about nine different types of abundance patterns in presolar SiC grains of which three are shown in Figure 10a-c. We previously modeled these patterns in terms of fractional condensation and discussed how the trace element abundances link SiC grains to different types of carbon stars [34].

Most of the observed patterns are characterized by depletions or enrichments of volatile elements (Sr, Ba) or highly refractory elements (e.g., Ti, Zr). The first step in the pattern analyses is to check if s-process elements are solar (C-J type like) or enriched (C-N type like). The calculations indicate that Ti and Zr are both highly refractory and that they should condense together. Thus, any increase in s-process elemental abundances is reflected by a Zr/Ti ratio that is higher than solar. This is observed for the carbides enclosed in presolar graphite grains from meteorites, where Zr/Ti ratios indicate enrichment of Zr up to ~30 times solar [76].

Once the abundances are obtained, comparison with calculations such as those shown in Figure 9 indicates how a particular pattern in SiC is established. For example, the patterns in Figure 10a require s-process element abundances 3-4 times solar. Comparison of the measured patterns in Figure 10a with those shown in Figure 9 also shows that gas-solid equilibrium stopped before Sr and Ba were fully condensed into the SiC grains.

In some cases, matching the observed SiC trace element patterns requires the removal of refractory Ti-Zr-C grains prior to SiC condensation because the SiC grains are depleted in refractory elements. This is the case for the patterns shown in Figures 10b and 10c. TiC condenses about ~50 K higher than SiC (for the P-T profiles shown in Figure 2), and TiC grains (containing other refractory carbides in solid solution) may have been lost from the SiC forming region in the CSE before the TiC grains were incorporated into SiC. Early isolation of such ultrarefractory TiC carbides grains is again indicated by the discovery of such grains in the presolar graphites isolated from meteorites [76]. Barium and Sr become enriched

414

in the gas relative to Y and Zr, which had condensed into the TiC grains. Upon cooling, condensation of SiC starts removing the remaining refractory elements from the gas. At lower temperatures Ba and Sr can also condense into the SiC. However, Sr is somewhat more volatile than Ba and apparently the SiC grains in Figure 10b never equilibrated at temperatures low enough to allow all Sr to condense into SiC. Thus, the patterns in Figure 10b show a relative Sr depletion. A similar scenario explains the patterns in Figure 10c, which show relative Ba enrichments and Sr depletions. The main difference with the pattern in Figure 10b is that overall s-process element enrichments are 10 times solar and that a larger fraction of refractory elements were removed before SiC formation (for detailed description of modeling these patterns see [34]).
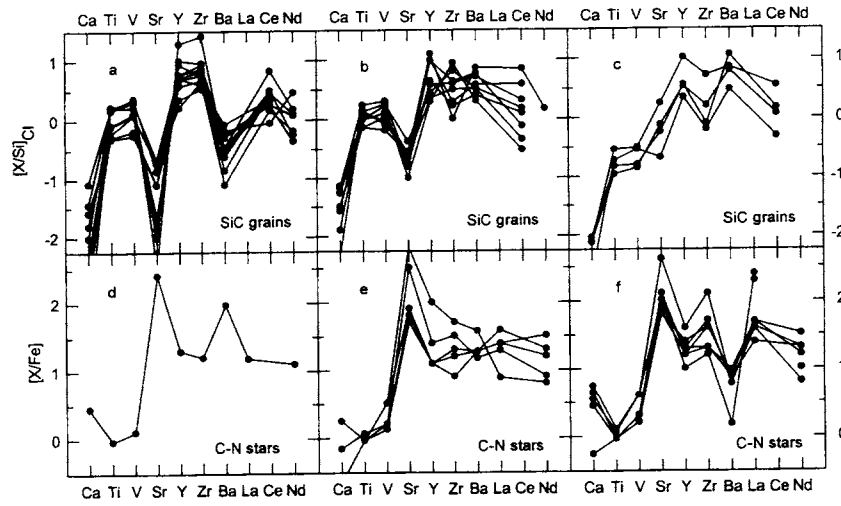
Figure 10. Top panel 10a-c: Measured trace element patterns in SiC grains isolated from meteorites from the work by Amari *et al.* [77]. Three out of nine different types of patterns are shown. The normalization is $[X/Si]_{Cl} = log (X/Si)_{grain}-log(X/Si)_{Cl-chondrites}.$ Bottom panel 10e-f: Abundances in N-stars from Utsumi [44] renormalized to solar abundance data of Anders & Grevesse [54]; notation is: $[X/Fe] = log(X/Si)_{star}-log(X/Si)_{solar}.$ Only elements common to both data sets are shown.

Amari *et al.* also measured low abundances of Ca, Fe, and Al in the SiC grains. These elements are expected to condense into SiC, assuming ideal solubility of CaS, Fe or Fe₃C and AlN (see discussion of Figure 9). The observed abundances, in particular those of Fe, are lower than the predicted abundances, indicating that the assumption of ideal solubility does not apply. The other possibility is that the elemental abundances of Al, Ca, and Fe may be subsolar in the N-stars where the SiC grains originated and not solar, as assumed in the calculations. The observations by Utsumi [44] and Lambert *et al.* [51] indicate that N-stars have Ca and Fe abundances close to solar. However, the N-stars from which the

presolar SiC grains originated more than 4.6 Gyrs ago may have had lower metallicities than present day N-stars. This issue needs further investigation.

The preceding discussion shows that the observed trace element patterns in circumstellar SiC grains are compatible with fractional condensation from a gas in carbon star CSE. Next we explore the consequences of fractional condensation for trace element abundances in carbon stars.

Trace element abundances in carbon star atmospheres

The different volatilities of trace elements lead to fractional condensation of more refractory elements into SiC and retention of more volatile elements in the gas. After the grains are expelled from the stellar atmosphere, the residual gas is relatively enriched in the more volatile elements which did not condense into SiC. In other words, fractional condensation can establish complementary trace element abundances in SiC grains and stellar atmospheres. This scenario is comparable to those for metal-poor post-AGB stars, which have either accreted dust-depleted matter from a binary companion via an accretion disk, or, in a single star scenario, have lost dust once a drop in AGB mass loss causes matter fall-back onto the star [96,97]. The latter, single star scenario seems more probable and suggests that radiation pressure drives refractory element bearing dust outward, while lack of dynamical support from the star after a drop in AGB mass-loss favors volatile rich-gas fall-back onto the star. The observed trace element abundances in N-stars are in accordance with such a scenario.

Abundances in cool stars are generally difficult to determine because of line blending. As a result, only very few data are available. We use abundance data determined by Utsumi [44] for 30 N, R, and J-stars. The R and J stars display relatively uniform, flat abundance patterns (Figure 1), but N-stars have several types of patterns. In addition to the patterns with uniform s-process element enrichments shown for four N-stars in Figure 1, other N-stars in Utsumi's sample have patterns displaying relative Sr and/or Ba enrichments. These patterns are shown in the bottom panel in Figure 10, where plots are arranged to show the complementary nature of the SiC grain and N-star abundance patterns. Volatile elements (Sr, Ba) are preferentially enriched in the stars and depleted in the SiC grains, while refractory elements are relatively depleted in the stars and enriched in the grains.

In Table 3 we summarize information about the 21 N-stars in Utsumi's sample. Of these 21 stars, four stars have patterns with approximately solar Ca, Ti, and V abundances and uniform s-process element enrichments. These patterns are normally taken as characteristic for N-stars (Figure 1). Thirteen other stars have abundance patterns complementary to those in SiC grains. These pattern are characterized by relative Sr and Ba enrichments (Figure 10d), relative Sr enrichments (Figure 10e), and relative Sr, Zr enrichments and Ba depletions (Figure 10f). Only

Table 3. N-Stars with Increased s-Process Element Abundances from Utsumi's Sample [44] Grouped By Their Abundance Patterns

Name (1)	HD (2)	Sp. T (3)	Sp. T. (4)	Var. (5)	P (days) (6)	R/R_{ph} (7)	dM/dt (8)	v_{exp} (9)	T_{eff} (K) (10)	$^{12}C/^{13}C$ (11)	C/O (12)	Tc (13)	LRS (14)	IRAS (15)	Notes
uniform s-process element enrichment (Figure 1)															
UU Aur	46687	N3	C5,6-	SRb	234	1.64	3.9e-6	12.9	2825	52	1.063	no	43	VII	amorph. C. emission
RR Her	144578	N0	C8,1e	SRb	240	...	...	2				...	...	...	
Z Psc	7561	N0	C5,4	SRb	144	...	4.9e-7	4.3	2870	55	1.014	...	41/22	VII	detached CSE?
S Sct	174325	N3	C5,5	SRb	148	...	5.4e-6	17.3	2895	45	1.069	...	1n	VIa	detached CSE. Binary?
s-process elements enriched, high Sr, high Ba (Figure 10d)															
19 TX Psc	223075	Nb	C5,4+	Lb	144/278	...	5.6e-7	10.7	3030	43	1.027	yes	1n	VIa	
s-process elements enriched, high Sr (Figure 10e)															
RS Cyg	192443	N0pe	C5.5,3e	SRa	418	...	...	...	...	...	...	(yes)	16	...	no dust. Binary?
W Ori	32736	N5	C5,5.5	SRb	212	1.16	6.2e-7	11.2	2680	79	1.16	...	44	VII	
BL Ori	44984	Nb	C5-,4+	Lb	...	...	1.0e-7	9.8	2960	57	1.039	yes	16	VII	no dust
V1942 Sgr	180953	N2	C5+,5.5	Lb	...	1.64	6.1e-7	10.0	2900	...	1.12	...	18	VIa	no extented atm.
VY UMa	92839	N0	C5,4.5	Lb	200::	1.38	4.8e-7	7.9	2855	44	1.060	yes	42	VIa	
s-process elements enriched, high Sr, high Zr, low Ba (Figure 10f)															
AQ And	2342	Nb	C5+,4.5	SR	346	1.56	...	...	...	...	...	...	42	VIa	
V Aql	177336	N6	C5,5	M/SRb	353	...	3.4e-7	9.2	2610	82	1.25	...	42	VIa	no Ba data
ST Cam	30243	N5	C5-,5.5	SRb	300	1.37	5.4e-7	10.5	2800	61	1.14	...	41/23	VII	Li-rich
UX Dra	183556	N0	C5,5	SRb	168	1.39	8.2e-7	6.0	2900	32	1.046	yes	4n	VII	
U Hya	92055	N2	C5,5-	SRb	310	1.42	5.0e-7	8.8	2825	32	1.043	yes	42	VIa	= V460 Cyg
DS Peg	206570	N1	C5,4.5	SRb	180	1.51	1.1e-6	10.9	2845	61	1.062	yes	42	VIa	amorph. C emission
Y Tau	38307	N2	C5-,5+	SRb	242	1.57	8.5e-7	11.6	2600	58	1.040	...	45	VII	
Stars with other ungrouped patterns															
X Cnc	76221	N3	C4,5.5.5	SRb	195	1.23	7.7e-7	9.7	2620	52	1.14	no	42	VII	like TX Psc but high La high Zr, low Sr & Ba
TU Gem	42272	N3	C5+,5-	SRb	230	...	1.1e-6	12.0	2770	59	1.12	(no)	4n	VII	high Zr, low Sr & Ba, am. C Ba high
SS Vir	108105	Np	C4.5,6-:e	M/SRa	364	...	1.7e-7	14.2	2300	...	1.08	no	...	...	
RV Mon	51620	NB/R9	C4,4	SRb	132	...	...	...	3000	...	...	...	43	...	

(1) & (2) GCVS name [100] and Henry Draper number. (3) & (4) Spectral classification [41]. RR Her, RV Mon from [44]. (5) & (6) Variable type and period in days [100,101]. (7) R/R_{ph} inner dust shell radius [95]. (8) & (9) Mass loss rates from CO ($M_\odot$/yr) and expansion velocities (km/s) [52,53,102]. (10) & (11) Effective temperatures [51-53]. (11) C-isotopes and C/O ratios from [51-53]. (13) Technetium present in spectrum [47]. (14) LRS: [56,102-105]. 1n: featureless blue spectrum, 2n,3n,6n: silicate 9.8 μm emission. 4n: SiC 11.3 μm emission. n: band strength increasing from 1-9. (15) IRAS: position in IRAS two color diagram [102-105].

four stars in the sample have abundance patterns for which we have not (yet?) identified complementary SiC grains.

We believe that the different stellar abundance patterns are not analytical artifacts. Utsumi [44] carefully selected bands free of blending and applied the same curve of growth method to all stars in his sample. He gives an uncertainty of 0.4 dex for solar normalized abundances (except for the REE, where uncertainties may be larger). Although absolute abundances may vary, we do not believe that the relative abundance patterns would change dramatically. It also seems unlikely that systematic errors in the analyses produce the variety of patterns. Kilston [43] also reports heavy element abundances for eight N-stars. Stars common to Kilston's and Utsumi's samples have similar abundances once both data sets are normalized to the same solar abundances. Unfortunately, Kilston did not present Sr abundances, which are necessary to establish the type of abundance patterns.

We searched for other stellar properties which may relate stars having similar abundance patterns. However, no obvious trends in spectral type, variable type, periods, location of the inner dust shell, mass-loss rates, gas expansion velocities, and effective temperatures are visible from the data in Table 3. Among the chemical signatures, the carbon isotopic composition and the C/O ratios are also inconclusive. One hint of a common grouping other than by abundance pattern is the presence or absence of Tc in their stellar spectra. Stars with unfractionated patterns (Figure 1) and the ungrouped stars (X Cnc, TU Gem, SS Vir, RV Mon) do not show Tc, while Tc is present in the stars with fractionated patterns (Figure 10d-f). However, the absence or presence of Tc needs to be checked for all stars in Utsumi's sample to decide if Tc is a tracer of the suggested groupings in Table 3.

The absence of Tc in RR Her, Z Psc, and S Sct could be a sensitive test for binarity [98]. Stars showing s-process element enhancement but lacking Tc, which is also indicative of third dredge up, may be part of a binary system. Mass transfer from the companion star in the past could have established the elemental abundances now observed. Such a scenario is suggested by Barnbaum *et al.* [99] for V Hya, and could also be the case for the stars in the first and last group in Table 3 where s-process elements are enriched and Tc is absent.

We suspect that binarity may be responsible for establishing the abundances in TU Gem and SS Vir (listed in bottom of Table 3). Their abundance patterns are characterized by depletions in Ba and Sr, opposite to the Ba and Sr enrichments predicted by fractional condensation. TU Gem and SS Vir may have accreted larger amounts of refractory dust than gas from a companion star. More detailed modeling is required to understand their abundance patterns.

The infrared properties of carbon stars may provide another way to group the stars in Table 3. The low resolution spectra (LRS) classification indicates that most of the stars display SiC emissions (LRS = 4n). However, among the stars having either Sr and Ba or Sr enrichments, some have featureless blue spectra (LRS = 1n). The presence of thin dust shells or even the absence of dust (LRS =

1n) may be problematic for a model which requires trace element removal into dust grains. Condensation during the variability cycle is required to effectively remove refractory elements into grains and enrich the gas in volatile elements. However, the current lack of observed dust shells does not imply that dust formation is not taking place in these stars. The very low expansion velocities and mass-loss rates for these stars may suggest that dust formation only takes place on undetectably small scales. An advantage of low dust abundances in the SR and Lb variables is that dust-gas momentum coupling may become less effective, so that the volatile enriched gas falls back onto the star while the radiation pressure accelerates the dust outwards.

Dust formation could also have occurred in an earlier time in these irregular pulsating variables. The introduction of the IRAS two-color diagram provides a guide to dust forming processes which may have occurred earlier [102-105]. Van der Veen & Habing 1988 [102] describe the far infrared excesses by plotting the 25 µm vs. the 60 µm excess and define characteristic regions for late type stars. Carbon stars typically plot into region VIa or VII of this IRAS two-color diagram. Of particular interest is the region VIa for Lb and SR variable stars with 60 µm excesses. This region is indicative of distant cool fossil dust shells implying that earlier evolutionary stages with higher mass loss rates have occurred in these stars. For example, the detached CSE of S Sct is well known [52,53] but no SiC is seen in emission (LRS = 1) indicating that no (observable) SiC formation is currently taking place. Thus, atmospheric trace element abundances cannot be altered by fractional condensation into SiC and trace elements appear unfractionated.

Stars with LRS = 1n are clustered among stars from Figure 10d & e while stars grouped in Figure 10f all have LRS = 4n. Old fossil shells occur among stars from all groups in Figure 10d-f. The LRS and IRAS properties are not correlated and no clear groupings are possible for the stars in Table 1 using their infrared properties. Since all these stars are probably at different stages in their evolution, yet another variable, namely long time evolution, needs to be considered. More data are needed to allow statistically significant modeling to reveal dust evolution around carbon stars.

CONCLUSIONS AND OUTLOOK

Thermochemical equilibrium calculations have been and still are a useful tool to model the chemistry in carbon star atmospheres. Emission bands of expected major element condensates are observed in carbon stars. Dust grains originating from these types of stars are identified in meteorites, showing that these grains survived their voyage through the ISM and thermal processing in the solar nebula and on meteorite parent bodies. The isotopic and trace element signatures of these grains leave no doubt of their carbon star parentage. Yet many questions remain about grain formation in stellar atmospheres. We conclude by pointing out some

419

areas where more information is needed to increase our understanding about grain formation processes.

Several physical properties of carbon stars such as temperature, pressure, or radius as a function of variability need to be better understood as these directly influence gas chemistry and condensation. Understanding the long term evolution of carbon stars and their dust shells is yet another challenge, for which their infrared properties may provide many more clues.

More observational data on chemical composition of carbon stars are needed. For example, the condensation calculations indicate that the C/O ratio of the gas decreases due to condensation of C-bearing dust during minimum of the variability cycle. Thus, determinations of C/O ratios in cool N type carbon stars may yield C/O ratios lower than the bulk gas & dust value. The determination of the C/O ratio at different stages in the variability cycle may reflect this variation and also provide information on the amount of dust produced between minimum and maximum light phase. Yet another check for dust formation as a function of variability could be obtained from infrared dust properties.

The existence of dust from carbon stars implies that dust formation (nucleation!) timescales and loss rates from the stellar atmosphere must be fast relative to the time interval between minimum (grain production) and maximum (potential grain evaporation). These constraints should be included in nucleation models. Also, nucleation models often call for supersaturation ratios >> 1 (i.e., condensation temperatures below the equilibrium values) Nevertheless, observations show dust present at stellar atmospheric distances compatible with those predicted by equilibrium thermodynamics.

The question of carbon star metallicity also needs further attention. What was the metallicity of the carbon stars providing the graphite and SiC grains to the solar nebula 4.6 Gyrs ago?

Trace element abundances (i.e., Sr, Ba, Zr, REE) need to be determined for more C-stars, ideally as a function of light curve. It would be interesting to see whether fractionated trace element patterns are restricted to SR and Lb variables or also occur in mira variables. Trace element abundances of the gas can become fractionated during condensation processes and depletions may be observable if abundances are determined as a function of lightcurve and SiC band strength.

More data about physical properties, chemical composition, and dust from less abundant carbon stars (e.g., H-rich CH stars and H-depleted HdC & R CrB type stars) are also desired since they may also have contributed to the presolar grains in meteorites.

REFERENCES

1. Secchi, A., *Compt. Rend. Acad. Sci., Paris* **66**, 124-126 (1868).
2. Pickering, E. C., *Harvard Ann.* **27**, 1 (1890).
3. Pickering, E. C., *Harvard Circ.* **145**, 1-4 (1908).
4. Rufus, W. C., *Publ. Astron. Obs. Univ. Michigan* **2**, 103-143 (1916).
5. Wildt, R., *Z. f. Physik* **5**, 856-879 (1929).
6. Cambresier, Y., and Rosenfeld, L., *MNRAS* **93**, 710-723 (1933).
7. Rosenfeld, L., *MNRAS* **93**, 724-729 (1933).
8. Wildt, R., *Z. f. Astrophysik* **6**, 345-354 (1933).
9. Russell, H. N., *ApJ* **79**, 317-342 (1934).
10. Bouigue, R., *Mem. Soc. Roy. Liege, Coll. 8°*, **18**, 346-351 (1957).
11. DeJager, C., and Neven, L., *Mem. Soc. Roy. Liege, Coll. 8°*, **18**, 357-394 (1957).
12. Cowley, A. P., *PASP* **74**, 223-229 (1962).
13. Hoyle, F., and Wickramasinghe, N. C., *MNRAS* **124**, 417-433 (1962).
14. Aller, L. H., *The atmospheres of the sun and stars*, New York: Ronald Press Co., 1963.
15. Tsuji, T., *Proc. Jpn. Acad.* **40**, 99-104 (1964).
16. Dolan, J. F., *ApJ* **142**, 1621-1632 (1965).
17. Morris, S., and Wyller, A. A., *ApJ* **150**, 877-907 (1967).
18. Donn, B., Wickramashinge, N. C., Hudson, J. P., and Stecher, T. P., *ApJ* **153**, 451-464 (1968).
19. Fix, J. D., *MNRAS* **146**, 37-49 (1969).
20. Fix, J. D., *MNRAS* **146**, 51-55 (1969).
21. Friedemann, C., *Physica* **41**, 139-143 (1969).
22. Gilman, R. C., *ApJ* **155**, L185-L187 (1969).
23. Tsuji, T., *A&A* **23**, 411-431 (1973).
24. Salpeter, E. E., *ApJ* **193**, 579-584 (1974).
25. Lucy, L. B., *ApJ* **205**, 482-491 (1976).
26. Clegg, R., and Wyckoff, S., *MNRAS* **179**, 417-432 (1977).
27. Lewis, J. S., and Ney, E. P., *ApJ* **234**, 154-157 (1979).
28. McCabe, E. M., Smith, R. C., and Clegg, R. E. S., *Nature* **281**, 263-266 (1979).
29. Clegg, R. E. S., *MNRAS* **191**, 451-455 (1980).
30. Lafont, S., Lucas, R., and Omont, A., *A&A* **106**, 201-213 (1982).
31. Shmeld, I. K., Strel'nitskii, V. S., and Gurvich, L V., *Sov. Astron. Lett.* **11**, 254-256 (1985).
32. Shmeld, I. K., *Sov. Astron.* **29**, 716-717 (1985).
33. Cherchneff, I., and Barker, J. R., *ApJ* **394**, 703-716 (1992).
34. Lodders, K., and Fegley, B., *Meteoritics* **30**, 661-678 (1995).
35. Sharp, C. M., and Wasserburg, G. J., *Geochim. Cosmochim. Acta* **59**, 1633-1652 (1995).
36. Helling, C, Jorgensen, U. G., Plez, B., and Johnson, H. R., *A&A* **315**, 194-203 (1996).
37. Keenan, P. C., *PASP* **105**, 905-910 (1993).
38. Yamashita, Y., *Tokyo Obs. Ann.* **13**, 169-217 (1972).
39. Yamashita , Y., *Tokyo Obs. Ann.* **14**, 47-59 (1975).
40. Keenan, P. C., and Morgan, W. W., *ApJ* **94**, 501-510 (1941).
41. Barnbaum, C., Stone, R. P. S., and Keenan, P. C, *ApJS* **105**, 419-473 (1996).
42. Shane, C. D., *Lick Obs. Bull.* **10**, 79, No. 329 (1920)
43. Kilston, S., *PASP* **87**, 189-206 (1985).
43. Utsumi, K., *Publ. Astr. Soc. Jpn.* **22**, 93-112 (1970).
44. Utsumi, K., *Proc. Jpn. Acad.* **61B**, 193-196 (1985).

45. Dominy, J. F., *ApJS* **55**, 27-43 (1984).

46. Dominy, J. J., *PASP* **97**, 1104-1111 (1985).

47. Little, S. J., Little-Marenin, I. R., and Hagen Bauer, W., *Astron. J.* **94**, 981-995 (1987).

48. Smith, V. V, and Lambert, D. L., *ApJ* **311**, 843-863 (1986).

49. Smith, V. V, and Lambert, D. L., *ApJS* **72**, 387-416 (1990).

50. Vanture, A. D., *ApJ* **381**, 278-287 (1991).

51. Lambert, D. L., Gustafsson, B., Eriksson, K., and Hinkle, K. H., *ApJS* **62**, 373-425 (1986).

52. Olofsson, H., Eriksson, K., Gustafsson, B., and Carlström, U., *ApJS* **87**, 267-304 (1993).

53. Olofsson, H., Eriksson, K., Gustafsson, B., and Carlström, U., *ApJS* **87**, 305-330 (1993).

54. Anders, E., and Grevesse, N., *Geochim. Cosmochim. Acta* **53**, 197-214 (1989).

55. Neugebauer, G., and Leighton, R.B., *Two-micron sky survey*, NASA SP-3047, pp. 309 (1969).

56. Neugebauer, G. *et al.*, IRAS catalogues and atlases, *A&AS* **65**, 607-1065 (1986).

57. Rosen, B., and Swings, P., *Ann. d' Astrophys. Fr.* **16**, 82-95 (1953).

58. Swings, P., *Ann. d' Astrophys. Fr.* **16**, 287 (1953).

59. Larimer, J. W., *Geochim. Cosmochim. Acta* **39**, 389-392 (1975).

60. Larimer, J. W., and Bartholomay, M., *Geochim. Cosmochim. Acta* **43**, 1455-1466 (1979).

61. Lattimer, J. M., Schramm, D. N., and Grossman, L., *ApJ* **291**, 230-249 (1978).

62. Gilra, D. P., and Code, A. D., *BAAS* **3**, 379 (1971).

63. Forrest, W. J., Gillett, F. C., and Stein, W. A., *ApJ* **195**, 423-440 (1975).

64. Little-Marenin, I.R., Ramsey, M.E., Stephenson, C.B., Little, S.J., and Price, S.D., *Astron. J.* **93**, 663-668 (1987).

65. Little-Marenin, I. R., *ApJ* **307**, L15-L19 (1986).

66. Willems, F. J., and deJong, T., *ApJ* **309**, L39-L42 (1986).

67. LeVan, P.D., Sloan, G.C., Little-Marenin, I.R., and Grasdalen, G.L., *ApJ* **392**, 702-705 (1992).

68. Thronson, H.A., Latter, W.B., Black, J.H., Bally, J., and Hacking, P., *ApJ* **322**, 770-786 (1987).

69. Epchtein, N., LeBertre, T., and Lepine, J. R. D., *A&A* **227**, 82-104 (1990).

70. Whittet, D. C. B., Duley, W. W., and Martin, P. G., *MNRAS* **244**, 427-431 (1990).

71. Ossenkopf, V., Henning, T., and Mathis, J. S., *A&A* **261**, 567-578 (1992).

72. Anders, E., and Zinner, E., *Meteoritics* **28**, 490-514 (1993).

73. Gallino, R., Busso, M., Picchio, G., and Raiteri, C. M., *Nature* **348**, 298-302 (1990).

74. Gallino, R., Raiteri, C. M., and Busso, M., *ApJ* **410**, 400-411 (1993).

75. Bernatowicz, T. J., Amari, S., Zinner, E. K., and Lewis, R. S., *ApJ* **373**, L73-L76 (1991).

76. Bernatowicz, T.J., Cowsik, R., Gibbons, P.C., Lodders, K., Fegley, B., Amari, S., and Lewis, R.S., *ApJ* **472**, 760-782 (1996)

77. Amari, S., Hoppe, P., Zinner, E., and Lewis, R. S., *Meteoritics* **30**, 679-693 (1995).

78. Lodders, K., and Fegley, B., *Earth Planet Sci. Lett.* **117**, 125-145 (1993).

79. Fegley, B., and Lodders, K., *Icarus* **110**, 117-154 (1994)

80. Glassgold, A. E., *Annu. Rev. Astron. Astrophys.* **34**, 241-277 (1996).

81. Bergeat, J., and Sibai, A. M., *A&A* **119**, 207-217 (1983).

82. LeBertre, T., *A&A* **190**, 79-86 (1988).

83. Gail, H. P., and Sedlmayr, E., *A&A* **171**, 197-204 (1987).

84. Gail, H. P., and Sedlmayr, E., *A&A* **206**, 153-168 (1988).

85. Lafon, J.-P.J., and Berruyer, N., *Astron. Astrophys. Rev.* **2**, 249-289 (1991).

86. Danchi, W. C., and Bester, M., *ApSS* **224**, 339-352 (1995).

87. Jorgensen, U. G., Johnson, H. R., and Nordlund, A., *A&A* **261**, 263-273 (1992).

88. Grevesse, N., and Noels A., in: *Origin and evolution of the elements*, Cambridge Univ. Press, 1993, pp. 14-25.

89. Kamijo, F., *Physica* **41**, 163-171 (1969).

90. Tabak, R. G., Hirth, J. P., Meyrick, G., and Roark, T. P., *ApJ* **196**, 457-463 (1975).

91. Martin, P. G., and Rogers, C., *ApJ* **322**, 374-392 (1987).

92. Orofino, V., Colangeli, L., Bussoletti, E., and Strafella, F., *ApSS* **138**, 127-140 (1987).

93. Orofino, V., Colangeli, L., Bussoletti, E., Blanco, A., and Fonti, S., *A&A* **231**, 105-110 (1990).

94. Jacob, K. T., and Seetharaman, S., *Met. Trans.* **25B**, 149-151 (1994).

95. Bergeat, J., Lefevre, J., Kandel, R., Lunel, M., and Sibille, F., *A&A* **52**, 245-261 (1976).

96. Mathis, J. S., and Lamers, H.J.G.L.M., *A&A* **259**, L39-L42 (1992).

97. Waters, L.B.F.M., Trams, N. R., and Waelkens, C., *A&A* **262**, L37-L40 (1992).

98. Alksne, Z., K., Alksnis, A. K., and Dzervitis, U. K., *Properties of galactic carbon stars*, Malabar, FL: Orbit Book Co., 1991, pp. 163.

99. Barnbaum, C., Morris, M., and Kahane, C., *ApJ* **450**, 862-875 (1995).

100. Khopolov, P. N. (ed. in chief), *General catalogue of variable stars*, Vol. I-IV, Moscow: Nauka, 1985-1987, pp. 1461.

101. Percy, J. R., Desjardins, A., Yu, L., and Landis, H. L., *PASP* **108**, 139-145 (1996).

102. van der Veen, W.E.C.J., and Habing, H.J., *A&A* **194**, 125-134 (1988).

103. Loup, C., Forveille, T., Omont, A., and Paul, J. F., *A&AS* **99**, 291-377 (1993).

104. Willems, F. J., *A&A* **203**, 51-64 (1988).

105. Willems, F. J., *A&A*, **203**, 65-70 (1988).